

# VLT/UVES and FORS2 spectroscopy of the GRB 081008 afterglow<sup>\*</sup>

V. D’Elia<sup>1,2†</sup>, S. Campana<sup>3</sup>, S. Covino<sup>3</sup>, P. D’Avanzo<sup>3</sup>, S. Piranomonte<sup>1</sup>, G. Tagliaferri<sup>3</sup>

<sup>1</sup> *INAF-Osservatorio Astronomico di Roma, Via Frascati 33, I-00040 Monteporzio Catone, Italy*

<sup>2</sup> *ASI-Science Data Centre, Via Galileo Galilei, I-00044 Frascati, Italy*

<sup>3</sup> *INAF, Osservatorio Astronomico di Brera, Via E. Bianchi 46, 23807 Merate (LC), Italy*

Accepted... Received...; in original form...

## ABSTRACT

We aim at studying the gamma-ray burst GRB 081008 environment by analysing the spectra of its optical afterglow. UVES/VLT high resolution spectroscopy of GRB 081008 was secured  $\sim 5$  hr after the *Swift*-BAT trigger. Our dataset comprises also three VLT/FORS2 nearly simultaneous spectra of the same source. The availability of nearly simultaneous high and low resolution spectra for a GRB afterglow is an extremely rare event. The GRB-Damped Lyman Alpha system at  $z = 1.9683$  shows that the interstellar medium (ISM) of the host galaxy is constituted by at least three components which contribute to the line profiles. Component I is the redmost one, and is 20 km/s and 78 km/s redward component II and III, respectively. We detect several ground state and excited absorption features in components I and II. These features have been used to compute the distances between the GRB and the absorbers. Component I is found to be  $52 \pm 6$  pc away from the GRB, while component II presents few excited transitions and its distance is  $200_{-80}^{+60}$  pc. Component III only features a few, low ionization and saturated lines suggesting that it is even farther from the GRB. Component I represents the closest absorber ever detected near a GRB. This (relatively) low distance can possibly be a consequence of a dense GRB environment, which prevents the GRB prompt/afterglow emission to strongly affect the ISM up to higher distances. The hydrogen column density associated to GRB 081008 is  $\log N_{\text{H}}/\text{cm}^{-2} = 21.11 \pm 0.10$ , and the metallicity of the host galaxy is in the range  $[\text{X}/\text{H}] = -1.29$  to  $-0.52$ . In particular, we found  $[\text{Fe}/\text{H}] = -1.19 \pm 0.11$  and  $[\text{Zn}/\text{H}] = -0.52 \pm 0.11$  with respect to solar values. This discrepancy can be explained by the presence of dust in the GRB ISM, given the opposite refractory properties of iron and zinc. By deriving the depletion pattern for GRB 081008, we find the optical extinction in the visual band to be  $A_V \sim 0.19$  mag. The Curve of Growth analysis applied to the FORS2 spectra brings column densities consistent at the  $3\sigma$  level to that evaluated from the UVES data using the line fitting procedure. This reflects the low saturation of the detected GRB 081008 absorption features.

**Key words:** gamma-rays: bursts – ISM: abundances – line: profiles – atomic data.

## 1 INTRODUCTION

Long gamma-ray bursts (GRBs) are powerful explosions occurring at cosmological distances, linked to the death of massive stars. The gamma-ray (or prompt) event is followed

by an afterglow at longer wavelengths, which is crucial in order to understand the physics of these sources, but also to investigate the nature of the interstellar medium (ISM) of high redshift galaxies. Before GRBs, such studies made use of Lyman-break galaxies (LBGs, see e.g. Steidel et al. 1999) and galaxies that happen to be along the lines of sight to bright background quasars, commonly referred to as QSO-Damped Lyman Alpha (DLA) systems. However, both classes are entangled by selection effects. In fact, LBGs fall in the bright end of the galaxy luminosity function and

<sup>\*</sup> Based on observations collected at the European Southern Observatory, ESO, the VLT/Kueyen telescope, Paranal, Chile, in the framework of the program 082-0755.

<sup>†</sup> E-mail: delia@asdc.asi.it

**Table 1.** UVES and FORS2 setups.

Instrument	Setup (nm)	Time from burst (hr)	Exposure (s)	Wavelength (Å)	Slit width	Resolution	S/N
UVES	Dic 1, 346	4.30	1800	3300 - 3870	1''	40 000	~ 3 - 5
UVES	Dic 1, 580	4.30	1800	4780 - 6810	1''	40 000	~ 5 - 8
FORS2	600B+22(A)	4.37	900	3300 - 6300	1''	780	~ 35 - 50
FORS2	600B+22(B)	4.63	900	3300 - 6300	1''	780	~ 35 - 50
FORS2	600B+22(C)	4.88	900	3300 - 6300	1''	780	~ 35 - 50
FORS2	A+B+C	4.63	2700	3300 - 6300	1''	780	~ 60 - 80

may not entirely represent typical high-redshift galaxies. On the other hand, QSO sightlines preferentially probe galaxy halos, rather than bulges or discs, for cross-section effects (Fynbo et al. 2008). Indeed, Savaglio et al. (2004; 2005) studied the ISM of a sample of faint *K*-band selected galaxies at  $1.4 < z < 2.0$ , finding MgII and FeII abundances much higher than in QSO systems but similar to those in gamma-ray burst hosts. Unfortunately, these galaxies are too faint to be spectroscopically studied up to higher redshifts, using 8m class telescopes. In this context, long GRBs can be used as torchlights to illuminate the high-redshift ISM, and thus represent an independent tool to study high-redshift galaxies.

Several papers report a metallic content in GRB host galaxies in the range  $10^{-2} - 1$  with respect to solar values (see e.g., Fynbo et al. 2006; Savaglio 2006; Prochaska et al. 2007). The GRB host metallicity is thus on average higher than in QSO-DLA systems, supporting the notion that GRBs explode well within their hosts. Since long GRBs are linked to the death of massive stars, they are thought to originate in molecular clouds. In this scenario, absorption from ground-state and vibrationally excited levels of  $H_2$  and other molecules is expected, but not observed (Vreeswijk et al. 2004; Tumlinson et al. 2007). The non-detection of these molecular states (with the exception of GRB 080607, see Prochaska et al. 2009; Sheffer et al. 2009) could be a consequence of the intense UV flux from the GRB afterglow, which photo-dissociates the molecules. However, molecular hydrogen is not detected in QSO-DLA either (e.g., Noterdaeme et al. 2008; Tumlinson et al. 2007), possibly indicating that these molecules are just hard to see at high redshift.

This is just an example of how a GRB can modify its surrounding medium. The most impressive manifestation of the transient nature of GRBs in optical spectroscopy is the detection of strong absorption features related to the excited levels of the OI, FeII, NiII, SiII and CII species and their time variability (Vreeswijk et al. 2007). This variability can not be explained assuming infrared excitation or collisional processes (Prochaska, Chen & Bloom 2006; Vreeswijk et al. 2007; D’Elia et al. 2009a), thus excitation by the intense GRB UV flux is the leading mechanism to produce these features. In this framework, the GRB/absorber distance can be evaluated comparing the observed ground state and excited level abundances with that predicted by time-dependent photo-excitation codes. This distance turns out to be in the range  $\sim 0.1 - 1$  kpc (Vreeswijk et al. 2007; D’Elia et al. 2009a,b; Ledoux et al. 2009).

Within the described framework, the best and most complete tool to perform these kind of studies is high resolution spectroscopy. In fact, it is the only way to disentangle the GRB interstellar medium in components and to separate the contribution to the absorption coming from the excited levels from the ground state ones. In addition, a high spectral resolution allows us to check for saturation of lines a few  $\text{km s}^{-1}$  wide that may appear unsaturated in lower resolution spectra (see e.g. Penprase et al. 2010).

In this paper we present data on GRB 081008, observed both in high and low resolution UVES and FORS2 at the VLT. The paper is organized as follows. Section 2 summarizes the GRB 081008 detection and observations from the literature; Sect. 3 presents the UVES observations and data reduction; Sect. 4 is devoted to the study of the features from the host galaxy, in particular their metallicity and distance from the GRB explosion site; Sect. 5 presents the FORS2 data and makes a comparison with the UVES ones; finally in Sect. 6 the results are discussed and conclusions are drawn. We assume a concordance cosmology with  $H_0 = 70 \text{ km s}^{-1} \text{ Mpc}^{-1}$ ,  $\Omega_m = 0.3$ ,  $\Omega_\Lambda = 0.7$ . Hereafter, with  $[X/H]$  we refer to the X element abundance relative to solar values.

## 2 GRB 081008

GRB 081008 was discovered by *Swift*/BAT on October 8, 2008, at 19:58:29 UT, and was detected by both the XRT and the UVOT instruments (Racusin et al. 2008). The UVOT magnitude in the white filter was reported to be 15.0 at 96 s from the trigger. The afterglow was also detected in all filters (from *B* to *K*) by SMARTS/ANDICAM  $\sim 4$  hr post burst (Cobb 2008). The redshift was secured by the Gemini-South/GMOS, which observed the afterglow 5 hr after the *Swift* trigger, reporting a redshift of  $z = 1.967$  (Cucchiara et al. 2008a). This value was later confirmed by our VLT/UVES+FOR2 data (D’Avanzo et al. 2008). The host galaxy was identified in the Gemini-South/GMOS acquisition image, and spectroscopically confirmed to be at the GRB redshift. The host of GRB 081008 has  $R = 20.75 \pm 0.01$ , which corresponds to an absolute AB magnitude of  $-21.5$  (Cucchiara et al. 2008b). A multi-wavelength study of the prompt event and the early afterglow phase of GRB 081008 is reported by Yuan et al. (2010, hereafter Y10), which present *Swift* (BAT+XRT+UVOT), ROTSE-III and GROND data.

**Table 2.** Rest frame equivalent widths of the UVES features.

Species	Transition	$W_r$ (Å)	$\Delta W_r$ (Å, $1\sigma$ )
OI <sup>3</sup> $P_2$ (g.s)	1302	0.57	0.05
AlII <sup>1</sup> $S_0$ (g.s)	1670	0.67	0.01
AlIII <sup>2</sup> $S_{1/2}$ (g.s)	1854	0.22	0.01
	1862	0.13	0.02
SiII <sup>2</sup> $P_{1/2}^0$ (g.s)	1260	0.63	0.07
	1808	0.20	0.02
SiII <sup>2</sup> $P_{3/2}^0$ (1*)	1264	0.63	0.07
	1816	0.06	0.02
CrII <sup>2</sup> $S_{1/2}$ (g.s.)	2056	0.20	0.02
	2062	0.14	0.02
	2066	0.11	0.02
FeIIa <sup>6</sup> $D_{9/2}$ (g.s)	2249	0.12	0.01
	2260	0.20	0.02
FeIIa <sup>6</sup> $D_{7/2}$ (1*)	1618	0.05	0.01
	1621	0.11	0.01
FeIIa <sup>6</sup> $D_{5/2}$ (2*)	1629	0.03	0.01
FeIIa <sup>6</sup> $D_{3/2}$ (3*)	1634	0.03	0.01
	1636	0.03	0.01
FeII5sa <sup>4</sup> $F_{9/2}$ (5*)	1637	0.04	0.01
	1612	0.12	0.01
	1702	0.21	0.02
FeIIa <sup>4</sup> $D_{7/2}$ (9*)	1635	0.03	0.01
NiII <sup>2</sup> $D_{5/2}$ (g.s.)	1741	0.07	0.02
NiII <sup>4</sup> $F_{9/2}$ (2*)	2166	0.19	0.01
	2217	0.27	0.01
	2223	0.09	0.02
ZnII <sup>2</sup> $S_{1/2}$ (g.s.)	2026	0.19	0.02
	2062	0.09	0.02

### 3 UVES OBSERVATIONS AND DATA REDUCTION

The GRB 081008 afterglow was observed with the high resolution UV-visual echelle spectrograph (UVES, Dekker et al. 2000), mounted at the VLT-UT2 telescope, in the framework of the ESO program 082.A-0755. Observations began on the 9<sup>th</sup> October 2008 at 00:16:43 UT ( $\sim 4.25$  hr after the *Swift*/BAT trigger), when the magnitude of the afterglow was  $R \sim 18.5$ . Data were acquired under good observing conditions, with seeing  $\sim 0.7$ . Only the UVES-dichroic-1 (red and blue arm) was used due to observational and scheduling constraints. The net exposure time of the observation is 30 minutes. The slit width was set to be  $1''$  (corresponding to a resolution of  $R = 40000$ ) and the read-out mode was rebinned to  $2 \times 2$  pixels. The spectral range of our observation is  $\sim 3300\text{Å}$  to  $\sim 3870\text{Å}$ ,  $\sim 4780\text{Å}$  to  $\sim 5750\text{Å}$ , and  $\sim 5830\text{Å}$  to  $\sim 6810\text{Å}$ . Table 1 makes a summary of our observations.

The data reduction was performed using the UVES pipeline (version 2.9.7, Ballester et al. 2000). The signal-to-noise ratio per pixel is  $\sim 3 - 5$  in the blue arm and

$\sim 5 - 8$  in the red one. The noise spectrum, used to determine the errors in the best-fit line parameters, was calculated from the real, background-subtracted spectrum, using line-free regions to evaluate the standard deviation of continuum pixels. Since the noise spectrum has been produced after the pipeline processing and the background subtraction, it takes into account possible systematic errors coming from the data reduction process. Fig. 1 shows the full, **smoothed and** normalized UVES spectrum.

### 4 UVES DATA ANALYSIS

The gas residing in the GRB host galaxy is responsible for many features observed in the GRB 081008 afterglow spectrum. Metallic features are apparent from neutral (OI) and low-ionization (AlII, AlIII, SiII, CrII, FeII, NiII, ZnII) species. In addition, strong absorption lines from the fine structure levels of SiII, FeII and from the metastable levels of FeII and NiII are identified, suggesting that the intense radiation field from the GRB excites such features. Table 2 gives a summary of all the absorption lines due to the host galaxy gas and report their rest frame equivalent widths ( $W_r$ ). The spectral features were analyzed with FIT-LYMAN (Fontana & Ballester 1995), using the atomic parameters given in Morton (2003). The probed ISM of the host galaxy is resolved into two main components separated by  $20 \text{ km s}^{-1}$  (Figs. 2 and 3). The wealth of metal-line transitions allows us to precisely determine the redshift of the GRB host galaxy. This yields a vacuum-heliocentric value of  $z = 1.9683 \pm 0.0001$ , setting the reference point to the redmost component (hereafter component I). The absorption features have been fitted with Voigt profiles, fixing the redshift of the two components when studying different lines. All transitions appear to be nicely lined-up in redshift, with the exception of component II of SiII $\lambda$ 1808. We attribute this misalignment to a contamination of another feature, and fit just the redmost side of component II. All ground state and metastable species present absorption features in both components, while fine structure levels in component I only. Two sharp features can be seen at  $v = \pm 80 \text{ km s}^{-1}$  from the FeII a<sup>6</sup> $D_{5/2}$  line (Fig. 2). They can not be separated in the FORS2 spectrum, thus we can not safely assess if they are real or not. The Doppler  $b$  parameter has been linked between different excited transitions belonging to the same species. A small variation of the Doppler parameter is allowed among different species, but the fits are quite good even fixing it. The values for components I and II are  $\sim 10$  and  $\sim 20 \text{ km s}^{-1}$ , respectively. An exception to this behaviour is represented by component II of ZnII. In order to obtain a good fit, a  $b \sim 4$  and  $\sim 50 \text{ km s}^{-1}$  is required for component I and II, respectively. This large  $b$  value in component II is necessary to adequately fit what appears as a low level of the continuum in particular in the ZnII $\lambda$ 2026 feature. **The large difference between the  $b$  parameters deduced for ZnII and CrII is odd, but we do not have a simple explanation for it.** The column densities and  $b$  parameters for all the elements and ions of the host galaxy's absorbing gas are reported in Table 3. A third component is actually identified at  $-78 \text{ km s}^{-1}$  for some low-ionization lines only, i.e., the OI $\lambda$ 1302, AlII $\lambda$ 1670 and SiII $\lambda$ 1260, and for the fine structure level SiII $\lambda$ 1264 (see

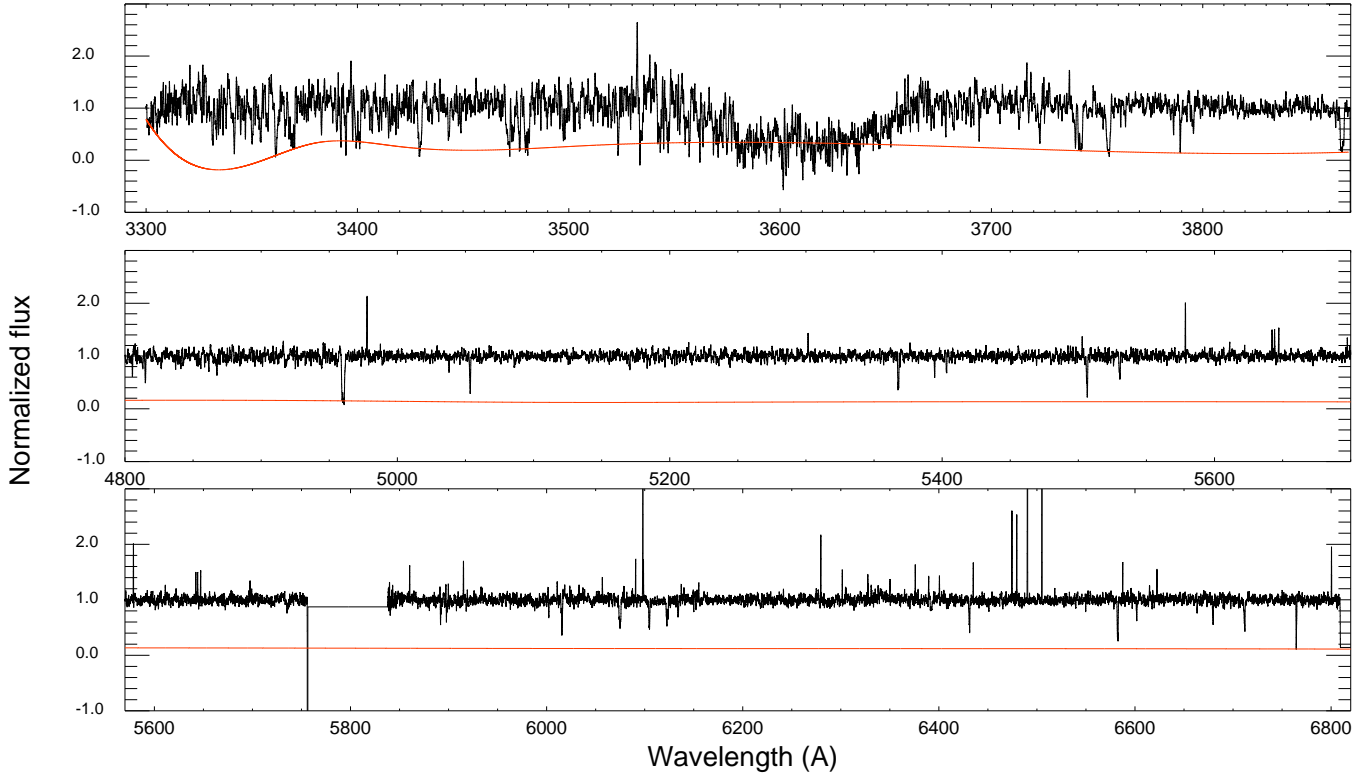


**Figure 1.** The full, **smoothed and** normalized UVES spectrum. Solid lines indicate the noise level as a function of wavelength.

Fig. 4). These lines are however heavily saturated, and their column densities reported in the table just set a lower limit to the true values. The reported upper limits are at the 90% confidence level.

#### 4.1 Abundances

The GRB081008 redshift was high enough to allow the hydrogen Ly $\alpha$  line to enter the UVES spectral window. Unfortunately, the UVES spectrum is extremely noisy in this region, and the derived hydrogen column density,  $\log(N_{\text{HI}}/\text{cm}^{-2}) = 21.33 \pm 0.12$  is quite uncertain. The fit is plotted in Fig. 5 (top panel) superimposed to the smoothed UVES spectrum. The fit is particularly poor on the wings, possibly because more than one component is needed to model the absorption. To obtain a better estimate of the column density, we used the FORS2 spectrum, that has a better S/N (see next section for details). The two component fit shown in Fig. 5 (bottom panel) gives a better representation of the data. **The two components are centered at  $z_1 = 1.944$  and  $z_2 = 1.975$ , respectively, and have column densities of  $\log(N_{\text{HI}}/\text{cm}^{-2}) = 20.82 \pm 0.14$  and  $\log(N_{\text{HI}}/\text{cm}^{-2}) = 20.79 \pm 0.12$ , respectively. The FORS2 total column density is  $\log(N_{\text{HI}}/\text{cm}^{-2}) = 21.11 \pm 0.10$ . This is our best fit result for  $N_{\text{H}}$  and will be used in the following.** The metallicity has been derived summing all non saturated component, excited level and ionic contributions belonging to the same atom, dividing these values by  $N_{\text{H}}$  and comparing them to the corresponding solar values given in Asplund et al. (2009). The upper limits of compo-

nent III result in an increment of the total column densities of  $< 20\%$  in the worst cases, so they were not included in the computation. The results are listed in Table 4. Column 2 reports the total abundance of each atom, while columns 3 and 4 report the absolute and solar-scaled  $N_X/N_{\text{H}}$  ratios, respectively, with  $X$  the corresponding element in column 1. Lower limits are reported whenever saturation does not allow us to securely fit the metallic column densities (see e.g., Fig. 4, where the line profiles reach the zero value of the normalized flux). In particular, for OI and AlII we considered also the values of the third, saturated component, while for SiII this has not been considered, since the fit to the SiII $\lambda$ 1260 resulted in a  $N$  value of component III which is considerably lower than that of components I and II. We derived metallicity values between 0.3 and 0.05 with respect to the solar ones. We caution, however, that many transitions belonging to other ionization states, which are commonly observed in GRB afterglow spectra could not be taken into account, because they are outside the UVES-dichroic-1 spectral range. In addition, the dust depletion can prevent the observation of part of the metallic content of the GRB081008 host galaxy. The reported relative abundances should then be considered as lower limits to the true GRB081008 metallicity. However, some considerations on higher ionization states are possible analyzing the FORS2 spectra, and dust content can be investigated through the study of the depletion pattern (see sects. 5 and 6).

**Table 3.** Absorption line logarithmic column densities for the three components of the main system, derived from the UVES spectrum.

Species	Observed transitions	N (cm <sup>-2</sup> )					
HI <sup>2</sup> S <sub>1/2</sub>	Lyα (UVES)	21.33 ± 0.12					
HI <sup>2</sup> S <sub>1/2</sub>	Lyα (FORS2)	21.11 ± 0.10					
	Components	20.82 ± 0.14	(z <sub>1</sub> = 1.944)			20.79 ± 0.12	(z <sub>2</sub> = 1.975)
Metals	Components	I (0 km s <sup>-1</sup> )		II (-20 km s <sup>-1</sup> )		III (-78 km s <sup>-1</sup> )	
Species	Observed transitions	N (cm <sup>-2</sup> )	b (km s <sup>-1</sup> )	N (cm <sup>-2</sup> )	b (km s <sup>-1</sup> )	N (cm <sup>-2</sup> )	b (km s <sup>-1</sup> )
OI <sup>3</sup> P <sub>2</sub>	λ1302	> 14.34	SAT	> 14.54	SAT	> 14.88	SAT
AlII <sup>1</sup> S <sub>0</sub>	λ1670	> 12.82	SAT	> 13.26	SAT	> 12.78	SAT
AlIII <sup>2</sup> S <sub>1/2</sub>	λ1854, λ1862	12.96 ± 0.04	12	13.04 ± 0.04	17	< 12.3	N/A
SiII <sup>2</sup> P <sub>1/2</sub> <sup>0</sup>	λ1260, λ1808	15.44 ± 0.03	9	15.08 ± 0.18	4	> 13.44	SAT
SiII <sup>2</sup> P <sub>3/2</sub> <sup>0</sup>	λ1264, λ1816	15.21 ± 0.05	9	< 15.0	N/A	< 15.0	N/A
CrII <sup>2</sup> S <sub>1/2</sub>	λ2056, λ2062, λ2066	13.51 ± 0.05	16	13.55 ± 0.04	21	< 13.3	N/A
FeII <i>a</i> <sup>6</sup> D <sub>9/2</sub>	λ2249, λ2260	15.09 ± 0.03	12	14.95 ± 0.04	20	< 14.7	N/A
FeII <i>a</i> <sup>6</sup> D <sub>7/2</sub>	λ1618, λ1621	13.95 ± 0.05	12	< 13.7	N/A	< 13.7	N/A
FeII <i>a</i> <sup>6</sup> D <sub>5/2</sub>	λ1629	13.71 ± 0.09	12	< 13.7	N/A	< 13.7	N/A
FeII <i>a</i> <sup>6</sup> D <sub>3/2</sub>	λ1634, λ1636	13.59 ± 0.09	12	< 13.5	N/A	< 13.5	N/A
FeII <i>a</i> <sup>4</sup> F <sub>9/2</sub>	λ1612, λ1637, λ1702	14.19 ± 0.05	12	13.76 ± 0.07	20	< 13.2	N/A
FeII <i>a</i> <sup>4</sup> D <sub>7/2</sub>	λ1635	13.35 ± 0.12	12	< 13.15	20	< 13.15	N/A
NiII <sup>2</sup> D <sub>5/2</sub>	λ1741	13.52 ± 0.08	12	13.33 ± 0.13	11	< 13.3	N/A
NiII <sup>4</sup> F <sub>9/2</sub>	λ2166, λ2217, λ2223	13.57 ± 0.02	12	13.27 ± 0.04	11	< 12.9	N/A
ZnII <sup>2</sup> S <sub>1/2</sub>	λ2026, λ2062	12.82 ± 0.06	4	12.87 ± 0.04	54	< 12.4	N/A

## 4.2 Excited levels

The level structure of an atom or ion is characterized by a principal quantum number  $n$ , which defines the atomic level, and by the spin-orbit coupling (described by the quantum number  $j$ ), which splits these levels into fine structure sub-levels. Excited features are routinely detected in GRB absorption spectroscopy, at the host redshift, due to the population of both  $n > 1$  and/or  $n = 1$  fine structure levels. GRB 081008 behaves the same way. In fact, component I features the first and second fine structure levels of the FeII ground state (*a*<sup>6</sup>D), the first fine structure level of the SiII <sup>2</sup>P<sup>0</sup>, and the FeII *a*<sup>4</sup>F<sub>9/2</sub>, FeII *a*<sup>4</sup>D<sub>7/2</sub>, NiII <sup>4</sup>F<sub>9/2</sub> metastable levels (the subscript represents the spin-orbit quantum number  $j$ ). Moreover, the FeII *a*<sup>4</sup>F<sub>7/2</sub> and NiII <sup>4</sup>F<sub>9/2</sub> excited states are also detected in component II (see Table 3 for details).

There is conspicuous literature on the population of excited states in GRB surrounding medium and their detection in the afterglow spectra (see e.g. Prochaska, Chen & Bloom 2006; Vreeswijk et al. 2007; D’Elia et al. 2010 and references therein). There is general consensus that these features are produced by indirect UV pumping by the afterglow, i.e., through the population of higher levels followed by the depopulation into the states responsible for the absorption features. This has been demonstrated both by the

detection of variability of fine structure lines in multi-epoch spectroscopy (Vreeswijk et al. 2007; D’Elia et al. 2009a), and through the column density ratios of different excited levels when multiple spectra were not available (Ledoux et al. 2009; D’Elia et al. 2009b).

Concerning GRB 081008, the high column density of the first metastable level of FeII (*a*<sup>4</sup>F<sub>9/2</sub>) with respect to the fine structure levels of the ground state can hardly be explained with a level population distribution given by a Boltzmann function (Vreeswijk et al. 2007), meaning that collisional excitations can be safely rejected. The lack of multi-epoch spectroscopy does not allow us to completely rule out the possibility that the exciting UV flux come from regions of high star-formation rates and not from the GRB. In fact, fine structure emission lines are present in Lyman-break, high redshift galaxies (see Shapley et al. 2003). If we assume that this flux comes from the GRB, we can estimate the GRB/absorber distance, comparing observed column densities to those predicted by a time-dependent, photo-excitation code for the time when the spectroscopic observations were acquired. The photo-excitation code is that used by Vreeswijk et al. (2007) and D’Elia et al. (2009a), to which we refer the reader for more details. Our equations take into account the  $(4\pi)^{-1}$  correction factor to the flux experienced by the absorbing gas described by Vreeswijk

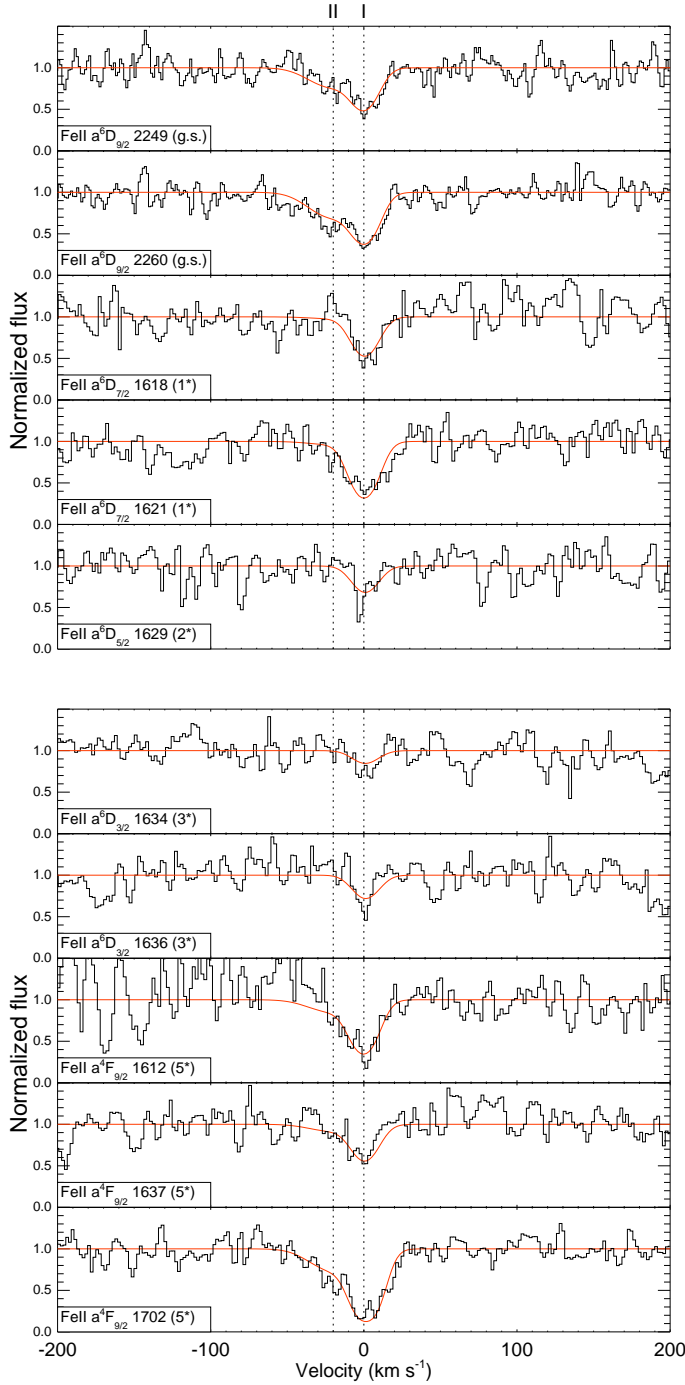


**Figure 2.** The FeII ground and excited absorption features. Solid lines represent the two Voigt components, best-fit model. Vertical lines identify the component velocities. The zero point has been arbitrarily placed at the redshift of the redmost component ( $z = 1.9683$ ). g.s. and  $n^*$  indicate ground state and  $n$ -th excited transitions, respectively.

(2011). We assume that the species for which we are running the code are at the ground state before the GRB blast wave reaches the gas. The GRB flux behavior before the UVES observation was estimated using the data in Y10 (lightcurve and spectral index), with no spectral variation assumed during the time interval between the burst and our observation. We concentrate on FeII and SiII levels be-

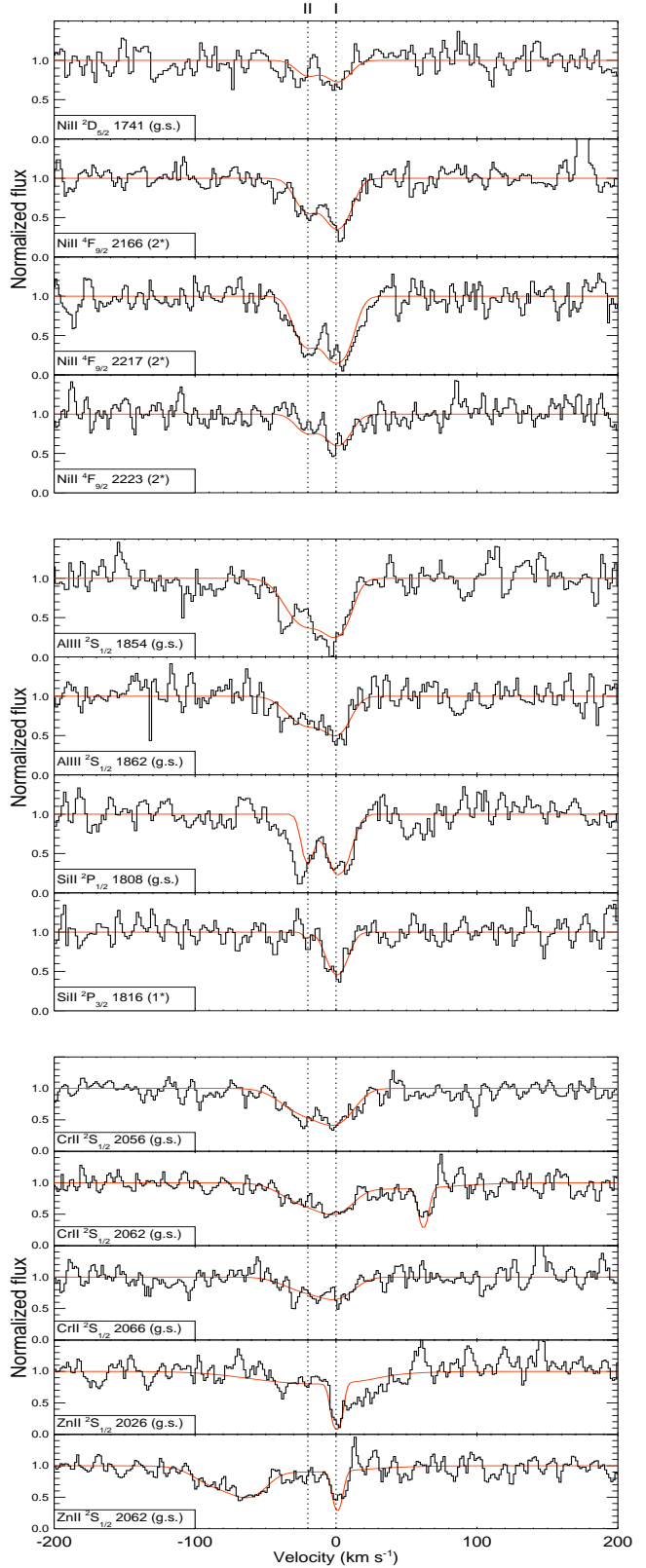


**Figure 3.** The NiII (top panel), AlIII and SiII, (middle panel), CrII and ZnII (bottom panel) absorption features. Solid lines represent the two Voigt components, best-fit model. Vertical lines identify the component velocities. The zero point has been arbitrarily placed at the redshift of the redmost component ( $z = 1.9683$ ). g.s. and  $n^*$  indicate ground state and  $n$ -th excited transitions, respectively.

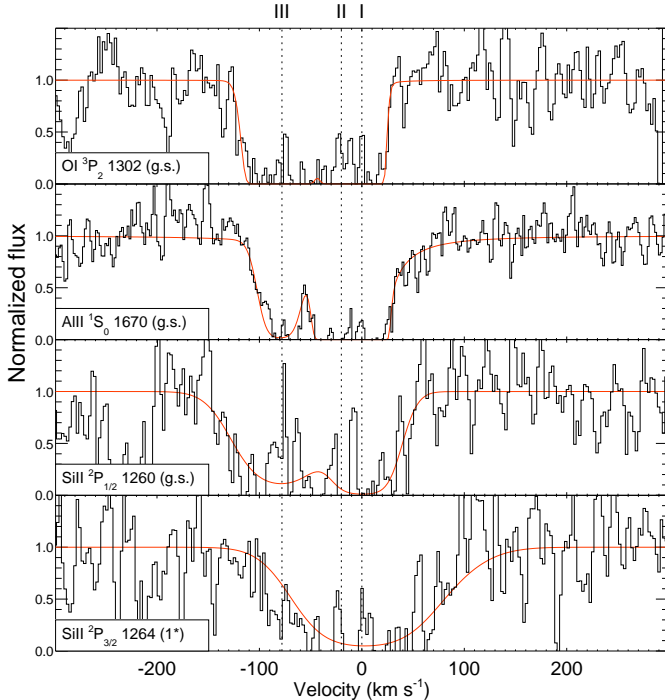


**Figure 4.** The O I  $\lambda$ 1302, Al III  $\lambda$ 1670, Si III  $\lambda$ 1260 ground state and Si III  $\lambda$ 1264 fine structure transitions. These lines need a three Voigt component model to be fitted and are heavily saturated. The zero point has been arbitrarily placed at the redshift of the redmost component ( $z = 1.9683$ ). g.s. and  $n^*$  indicate ground state and  $n$ -th excited transitions, respectively.

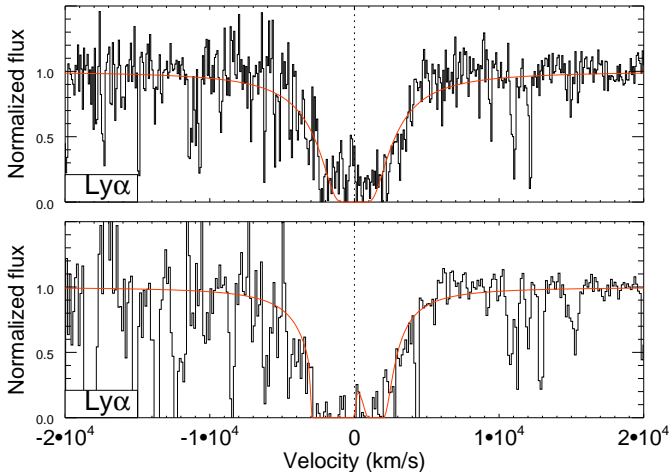


**Figure 5.** The Ly $\alpha$  absorption feature at the GRB081008 redshift. Top panel shows the single Voigt component, best-fit model for the UVES spectrum. Bottom panel shows the double component, best-fit model for the FORS2 spectrum. **The UVES fit is poor, while the FORS2 one gives a more reliable description of  $N_H$ .**

cause the NiII ground state has column densities not far from the 90% confidence level of  $\log(N_{NiII}/\text{cm}^{-2}) = 13.3$ , and thus the uncertainties on such values are high (Table 3). In addition, NiII ground state is detected only through the  $\lambda$ 1741 transition, because the lower oscillator strengths of the  $\lambda$ 1709 and 1751 lines prevents a detection of these features above the 90% level. The initial column densities of

**Table 4.** Metallicity computed from the UVES data.

Element $X$	$\log N_X/\text{cm}^{-2}$	$\log N_X/N_H$	$[X/H]$
O	$> 15.12 \pm 0.06$	$> -5.99 \pm 0.13$	$> -2.68 \pm 0.11$
Al	$> 13.70 \pm 0.04$	$> -7.41 \pm 0.13$	$> -1.86 \pm 0.11$
Si	$15.75 \pm 0.04$	$-5.32 \pm 0.12$	$-0.87 \pm 0.10$
Cr	$13.83 \pm 0.03$	$-7.28 \pm 0.08$	$-0.92 \pm 0.10$
Fe	$15.42 \pm 0.04$	$-5.69 \pm 0.13$	$-1.19 \pm 0.11$
Ni	$13.74 \pm 0.07$	$-7.37 \pm 0.13$	$-1.29 \pm 0.12$
Zn	$13.15 \pm 0.04$	$-7.96 \pm 0.13$	$-0.52 \pm 0.11$

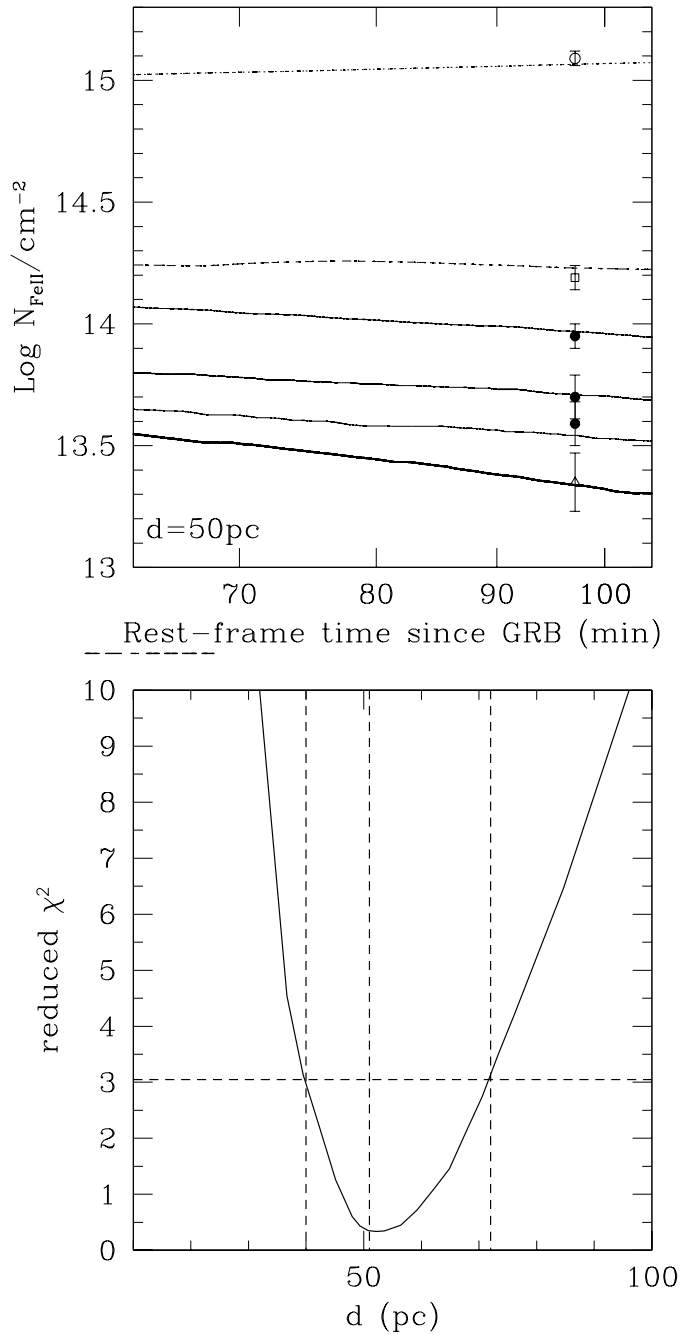
the ground states were computed from the observed column densities of all the levels of each ion, i.e., we are assuming that the species are not excited at  $t = 0$ . The initial values for FeII and SiII are  $\log(N_{SiII}/\text{cm}^{-2}) = 15.63 \pm 0.03$  and  $\log(N_{FeII}/\text{cm}^{-2}) = 15.21 \pm 0.02$  for component I, and  $\log(N_{FeII}/\text{cm}^{-2}) = 14.98 \pm 0.04$  for component II. Finally, the Doppler parameter used as input of this model has been left free to vary between 10 and 20  $\text{km s}^{-1}$ , i.e. the range of values that best fit the absorption features of components I and II.

Fig. 6 (top) shows the model that best fits the FeII data, obtained for a distance of 50 pc and a Doppler parameter of 20  $\text{km s}^{-1}$ . Fig. 6 (bottom) reproduces the behaviour of the reduced  $\chi^2$  as a function of the distance GRB/absorber. The distance of component I from the GRB explosion site results  $d_{I,FeII} = 51_{-11}^{+21}$  pc at the 90% confidence level. The same calculation was performed using the SiII atomic data. The results are displayed in Fig. 7, and the estimated distance is  $d_{I,SiII} = 52 \pm 6$  pc, which is consistent with what was estimated using the FeII data.

For component II, we have much less excited transitions. Fig. 8 shows the model which best fits the FeII data and the two theoretical curves compatible within the error bars for the FeII  $\alpha^4 F_{9/2}$  excited level column density, which is actually the only one with a positive detection in component II. The resulting distance between the GRB and this absorbing component is  $d_{II,FeII} = 200_{-80}^{+60}$  pc (90% confidence level), a larger value than  $d_I$ , as expected given the lack of excited transition in component II.

## 5 FORS2 SPECTROSCOPY

In the framework of the ESO program 082.A-0755, we observed the afterglow of GRB081008 also with the FORS2 low resolution spectrograph ( $R = 780$ ), mounted on VLT/UT1. We took three spectra of 900 s each, starting around Oct 09 at 00:20 UT (about 4.4 hours after the burst). We used the 600B grism, whose spectral coverage is 330–630 nm. The extraction of the spectra was performed within the MIDAS environment. Wavelength and flux calibration of the three spectra were obtained by using the helium-argon lamp and observing spectrophotometric stars. Tab. 1 reports a summary of our FORS2 observations. We searched for variability in the  $W_r$  of the FORS2 absorption lines, but we found none at the  $2\sigma$  level. This is not surprising, since fine structure and excited lines are expected to vary by less than  $\sim 0.05$  decades (in column density) during the acquisition time of the FORS2 spectra, which is  $\sim 15$  min rest frame (see Figs. 6-8). Since no variability is detected, we co-added



**Figure 6.** Top panel: FeII column densities for the ground level (open circle), fine structure levels of the ground state (filled circles), first metastable (open square) and second metastable (open triangle) transitions for component I in the spectrum of GRB 081008. Column density predictions from our time-dependent photo-excitation code are also shown. They refer to the ground level (dotted line), fine structure level (solid lines), first and second excited level (dashed and thick solid lines, respectively) transitions, in the case of an absorber placed at 50 pc from the GRB. Bottom panel: the reduced  $\chi^2$  as a function of the distance for the model reproduced in the upper panel. Dashed lines indicate the best fit distance and enclose the 90% confidence range.

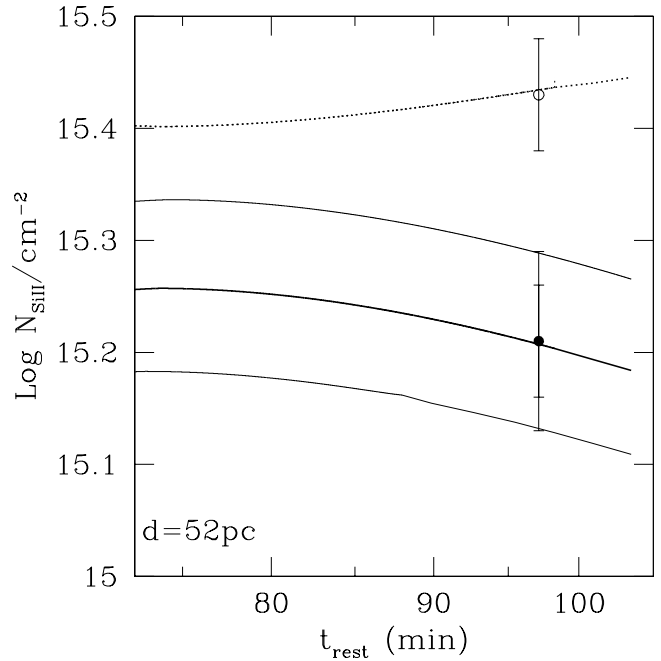


**Figure 7.** The SiII column densities for the ground level (open circle) and first fine structure level (filled circle) transitions for component I in the spectrum of GRB 081008. Column density predictions from our time-dependent photo-excitation code are also shown. They refer to the ground level (dotted line) and first fine structure level (thick solid line) transitions, in the case of an absorber placed at 52 pc from the GRB. The two thin solid lines display the models which enclose the fine structure level data at the 90% confidence level (error bars for this transition are drawn both at  $1\sigma$  and 90% confidence levels).

the three spectra, to improve the signal-to-noise ratio of our data, to obtain a value of  $\sim 60 - 80$  at  $\lambda > 4000\text{\AA}$ . The resulting spectrum is presented in Fig. 9, together with the spectral features identified at  $z = 1.97$ , a redshift consistent with that estimated using the UVES data. A list of the features detected in the FORS2 spectrum is reported in the first column of Table 5.

The Voigt fitting procedure is not adequate to compute the column densities of metallic species in low resolution spectroscopy. In this case, the Curve of Growth (COG) analysis (see e.g. Spitzer 1978) must be applied. For weak absorption lines, with width  $W_r < 0.1\text{\AA}$ , and for Doppler parameters  $b > 20 \text{ km s}^{-1}$ ,  $W_r$  is proportional to the column density  $N$ , and virtually insensitive to the Doppler parameter itself. For stronger lines this does not hold any more, and the relation between  $W_r$  and  $N$  is described by a COG, which is a function of  $b$ . In order to fit the correct COG to the data and to estimate  $b$ , different transitions (with different oscillator strengths  $f$ ) of the same species are needed. Following Spitzer (1978), we built up a code to perform this fit on our FORS2 data. To test our code, we compute  $W_r$  for all the UVES transitions featuring two components, and apply our fitting program. The result of the fit is shown in Fig. 10 (top panel), and the estimated column densities are reported in Table 6 (errors are given at the  $1\sigma$  level).

The effective Doppler parameter evaluated from the fit,  $b = 23 \text{ km s}^{-1}$ , is compatible with that estimated using the



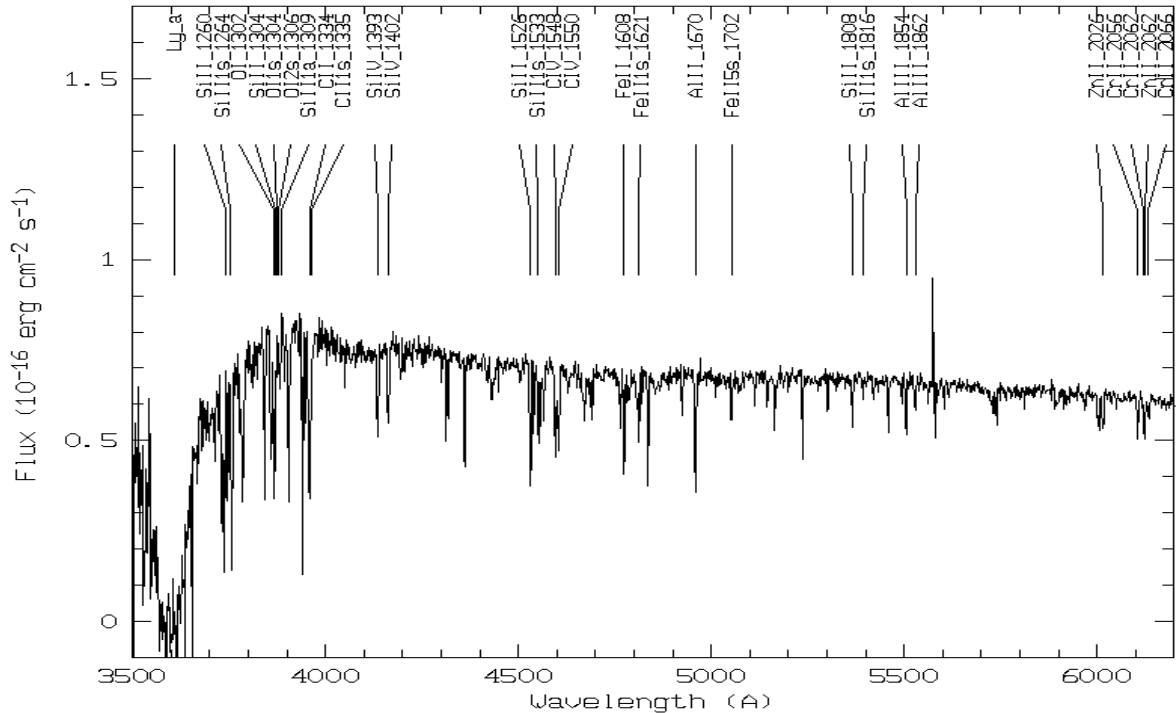


**Figure 9.** The flux-calibrated, co-added FORS2 spectrum of the GRB081008 afterglow, together with the spectral features identified at  $z = 1.9683$ .

line fitting profile. To compare the column densities estimated with the two methods, we sum for each species the contribution coming from the two components using the line fitting method (see values in Table 3), and report the results in Table 6. The agreement between line fitting and COG analyses is very good: each column density is within  $1\sigma$  from the corresponding value estimated using the other method. The only exception is the FeII5s, whose column density values however overlap at the  $2\sigma$  level.

We now apply the COG analysis to the FORS2 spectrum. First of all, we compute the  $W_r$  from the data. As shown in Table 5, despite the identification of nearly 30 transitions, reliable  $W_r$  can be evaluated only for 13 (second column of the table). This is because the lower FORS2 resolution does not enable to separate many of these transitions which are blended with each other. We then run the COG code using the FORS2  $W_r$ , and evaluate the corresponding column densities. The results are shown in the third column of Table 5, while the last column shows the UVES column densities for comparison. Errors are again at the  $1\sigma$  level, and Fig. 10 (bottom panel) shows the graphical output of the fit. The effective Doppler parameter estimated ( $b = 31 \pm 2 \text{ km s}^{-1}$ ) reproduces quite well the combination of the values computed for component I and II ( $\sim 10$  and  $\sim 20 \text{ km s}^{-1}$ , respectively, separated by  $\sim 20 \text{ km s}^{-1}$ ) using the line fitting method. The FORS2 and UVES spectra give consistent column densities, with the  $3\sigma$  confidence regions overlapping in the worst cases.

## 6 CONCLUSIONS AND DISCUSSION

In this paper we present high and low resolution spectroscopy of the optical afterglow of GRB081008, observed using UVES and FORS2 spectrographs at the VLT  $\sim 5$  hr after the trigger. We detect several absorption features (both neutral and excited) at the common redshift of  $z = 1.9683$ . The spectra show that the gas absorbing the GRB afterglow light can be described with three components identified in this paper as I, II and III, according to their decreasing velocity values.

We estimated the distances between the GRB and the absorbers. We find a distance for component I of  $d_{FeII,I} = 51_{-11}^{+21}$  pc and  $d_{SiII,I} = 52 \pm 6$ , using FeII and SiII, respectively. The SiII leads to a smaller uncertainty because its fine structure level is more sensitive to the flux experienced by the absorber. Other papers mainly use FeII as distance estimator, so for a safer comparison is better to consider our FeII value. For component II, this distance is greater,  $d_{II} = 200_{-80}^{+60}$  pc. We stress that these values are obtained assuming a three component absorber. However, we can not exclude a higher number of components, because our spectrum has a low S/N and a limited resolution. Component II is far away from GRB than component I, as expected given the lack of fine structure lines in this absorber. Component III does not show excited levels at all, and only shows low ionization states. Therefore, this is produced by an absorber located even farther from the GRB, in a region which is not significantly influenced by the prompt/afterglow emission.

Component I of GRB081008 is the closest to a GRB ever recorded. In fact, for the 6 other GRBs for which the GRB/absorber distance have been estimated, the closest

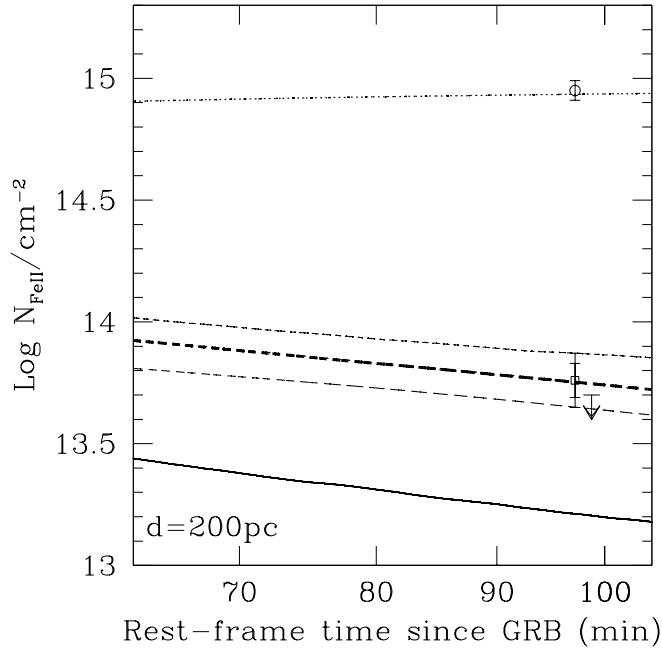


**Figure 8.** The Fe II column densities for the ground level (open circle), first fine structure level (upper limit) and first excited level (open square) transitions for component II in the spectrum of GRB 081008. Column density predictions from our time-dependent photo-excitation code are also shown. They refer to the ground level (dotted line), first fine structure level (solid line) and first excited level (thick dashed line) transitions, in the case of an absorber placed at 200 pc from the GRB. The two thin dashed lines display the models which enclose the excited level data at the 90% confidence level (error bars for this transition are drawn both at  $1\sigma$  and 90% confidence levels).

components are at  $d = 80\text{--}700$  pc from the GRB (Vreeswijk et al. 2007; D’Elia et al. 2009,a,b; Ledoux et al. 2009; D’Elia et al. 2010; Thöne et al. 2011). The values reported in literature have been corrected for the  $4(\pi)^{-1/2}$  factor discussed by Vreeswijk (2011). This behaviour can be interpreted as due to a dense environment close to the GRB explosion site. This high density is possibly witnessed by the a non negligible dust amount (see below) and by the metal content of the GRB surrounding medium. In fact, the GRB 081008 surroundings have the highest metallicity and the highest abundances of, e.g., Fe II and Ni II, among this sub-sample of GRBs. This high density in the GRB surroundings could constitute a barrier to the GRB prompt/afterglow emission, that is not able to strongly excite the interstellar medium up to the distances reached by the other GRBs.

The neutral hydrogen column density is  $\log(N_{\text{H,opt}}/\text{cm}^{-2}) = 21.11 \pm 0.10$ , while that estimated from *Swift* XRT data is  $\log N_{\text{H,X}}/\text{cm}^{-2} = 21.66^{+0.14}_{-0.26}$  (Campana et al. 2010). The latter value is for a solar abundance medium. Using  $N_{\text{H,opt}}$  we evaluate the GRB 081008 host galaxy’s metallicity. The values we find are in the range  $[X/H] = -1.29$  to  $-0.52$  with respect to the solar abundances. This value lies in the middle of the GRB distribution, (Savaglio 2006; Prochaska et al. 2007; Savaglio, Glazebrook & Le Borgne, 2009). From X-ray data a limit of  $[X/H] > -1.83$  (90% confidence limit) can be set assuming

**Table 5.** GRB081008 absorption features detected in the FORS2 spectrum, together with their  $W_r$  and column densities. UVES data are shown for comparison.

Transition	$W_r$ (Å) <sup>a</sup>	$N^b$	UVES $N^b$
CIIλ1334	BLEND	-	-
CIVλ1548	BLEND	-	-
CIVλ1550	BLEND	-	-
OIλ1302	BLEND	-	SAT
OIλ1304	BLEND	-	-
OIλ1306	BLEND	-	-
AlIIλ1670	0.74	$14.60^{+0.26}_{-0.20}$	SAT
AlIIλ1854	0.30	$13.42 \pm 0.02$	$13.30 \pm 0.03$
AlIIλ1862	0.17	$13.42 \pm 0.02$	$13.30 \pm 0.03$
SiIIλ1260	BLEND	$15.74^{+0.15}_{-0.11}$	$15.60 \pm 0.04$
SiIIλ1304	BLEND	$15.74^{+0.15}_{-0.11}$	$15.60 \pm 0.04$
SiIIλ1526	0.67	$15.74^{+0.15}_{-0.11}$	$15.60 \pm 0.04$
SiIIλ1808	0.25	$15.74^{+0.15}_{-0.11}$	$15.60 \pm 0.04$
SiII λ1264	BLEND	$15.17 \pm 0.01$	$15.21 \pm 0.05$
SiII λ1309	BLEND	$15.17 \pm 0.01$	$15.21 \pm 0.05$
SiII λ1533	BLEND	$15.17 \pm 0.01$	$15.21 \pm 0.05$
SiII λ1816	0.07	$15.17 \pm 0.01$	$15.21 \pm 0.05$
SiIV λ1393	0.47	-	-
SiIV λ1402	0.40	-	-
CrIIλ2056	0.27	$13.94 \pm 0.02$	$13.83 \pm 0.03$
CrIIλ2062	BLEND	$13.94 \pm 0.02$	$13.83 \pm 0.03$
CrIIλ2066	0.17	$13.94 \pm 0.02$	$13.83 \pm 0.03$
FeIIλ1608	0.54	$15.29^{+0.13}_{-0.10}$	$15.33 \pm 0.02$
FeIIλ1621	BLEND	-	$14.95 \pm 0.04$
FeIIλ1629	BLEND	-	$14.95 \pm 0.04$
FeIIλ1702	0.24	$14.16 \pm 0.02$	$14.33 \pm 0.05$
ZnIIλ2026	0.24	$13.22 \pm 0.02$	$13.15 \pm 0.04$
ZnIIλ2062	BLEND	$13.22 \pm 0.02$	$13.15 \pm 0.04$

<sup>a</sup> The error on  $W_r$  is  $0.01\text{Å}(1\sigma)$ .

<sup>b</sup> All values of the column densities are logarithmic (in  $\text{cm}^{-2}$ ).

a solar abundance pattern and requiring that the absorbing medium is not Thomson thick. If we set the metallicity to  $[X/H] = -0.5$ , the absorbing column density in the X-rays is higher, namely,  $\log N_{\text{H,X}}/\text{cm}^{-2} = 22.24^{+0.19}_{-0.30}$  and higher for lower metallicities. Fynbo et al. (2009) and Campana et al. (2010) show that in GRBs with a detectable Ly $\alpha$  feature (i.e., those at  $z > 2$ )  $N_{\text{H,X}}$  is on average a factor of 10 higher than  $N_{\text{H,opt}}$ , and GRB 081008 follows this trend. The intense GRB flux, which ionizes the hydrogen and prevents part of it to be optically detected, is the

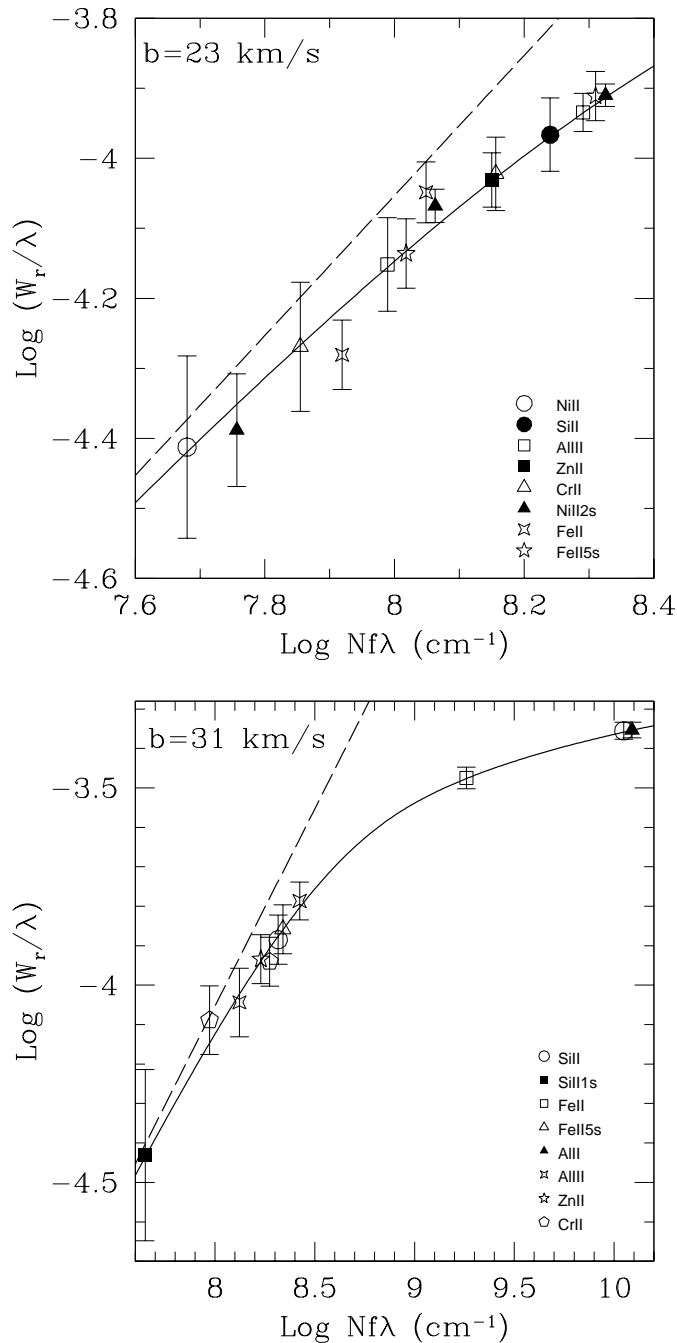


**Figure 10.** Top panel: the COG analysis tested using the UVES species featuring two components. Bottom panel: COG analysis applied to the FORS2 lines with a measured  $W_r$ . Solid lines represent the best fit obtained using the reported  $b$  values. Dashed lines show the  $b = \infty$  curve for comparison. The COG fits component I and II together in both plots.

common explanation for this discrepancy (Fynbo et al. 2009; Campana et al. 2010; Schady et al. 2011).

It is worth noting that observed abundances of FeII and ZnII are significantly different ( $[\text{Fe}/\text{H}] = -1.29 \pm 0.11$  and  $[\text{Zn}/\text{H}] = -0.52 \pm 0.11$ ). This can be ascribed to the different refractory properties of the two elements, with the former that preferentially tends to produce dust grains while

**Table 6.** Comparison between UVES column densities evaluated with the line fitting and COG methods.

Specie	N (COG analysis)	N (Line fitting)
AlIII	$13.29^{+0.05}_{-0.10}$	$13.30 \pm 0.03$
SiII	$15.66^{+0.06}_{-0.12}$	$15.60 \pm 0.03$
CrII	$13.83^{+0.03}_{-0.07}$	$13.83 \pm 0.03$
FeII (g.s.)	$15.31^{+0.01}_{-0.07}$	$15.33 \pm 0.02$
FeII $a^4F_{9/2}$	$14.13^{+0.07}_{-0.11}$	$14.33 \pm 0.05$
NiII (g.s.)	$13.81^{+0.01}_{-0.03}$	$13.74 \pm 0.07$
NiII $a^4F_{9/2}$	$13.73^{+0.05}_{-0.09}$	$13.75 \pm 0.02$
ZnII	$13.14^{+0.05}_{-0.10}$	$13.15 \pm 0.04$

All values are logarithmic (in  $\text{cm}^{-2}$ ).

the latter prefers the gas phase. The comparison between these ‘opposite’ elements can thus provide information on the dust content in the GRB environments. In order to be more quantitative, we derive the dust depletion pattern for the GRB081008 environment, following the method described in Savaglio (2000). We consider the four depletion patterns observed in the Milky Way, namely, those in the warm halo (WH), warm disk + halo (WHD), warm disk (WD) and cool disk (CD) clouds (Savage & Sembach 1996). We find that the best fit to our data is given by the WH cloud pattern, with a metallicity of  $\log Z_{\text{GRB}}/Z_{\odot} \sim -0.5$  and a GRB dust-to-metal ratio comparable to that of the WH environment, e.g.,  $d/d_{\text{WH}} = 1$  (Fig. 11). This metallicity value is consistent with our  $[\text{Zn}/\text{H}]$  measurement. This agreement is self-consistent with the use of zinc as a good indicator of metallicity. Since the latter quantity is linked to the extinction (see e.g., Savaglio, Fall & Fiore 2003) we derive  $A_V \sim 0.19$  mag along the GRB081008 line of sight. We check this value by modeling the flux-calibrated FORS2 spectrum. The SED is dominated by the Ly $\alpha$  which is difficult to model given the high fluctuations and other absorption lines. Anyway, the inferred  $A_V$  value is low and compatible with that evaluated from the dust depletion.

Another hint of dust is the non detection of FeII in the third component. The FeII column densities in components I and II are very similar, and this lets us believe that in component III the iron is present as well, but in the dust form. The higher presence of dust in components far away from the GRB has already been pointed out by D’Elia et al. (2007). They report a possible presence of dust in component III of GRB 050730, while the closer component II (featuring FeII fine structure lines) shows more iron in the gas state. The detection of more dust far away from the GRB can be explained since dust grains containing iron tends to be efficiently destroyed during a blast wave occurring after a GRB explosion (Perna, Lazzati & Fiore 2003).

The analysis of the FORS2 spectra extends our surveyed wavelength range, allowing the detection of higher ionization species, such as CIV and SiIV. Anyway, line profiles of high and low ionization species rarely match in redshift space and often if they do, it is because the line blending

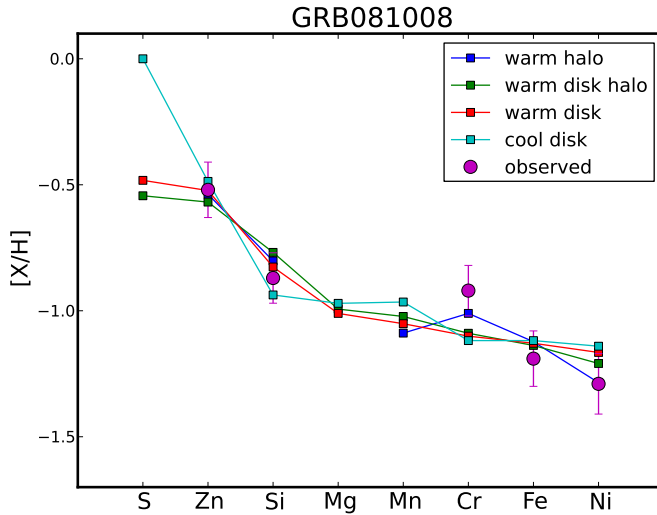


**Figure 11.** Depletion patterns in the absorbing gas of GRB 081008. Filled squares are taken from average gas-phase abundance measurements in warm halo (blue), warm disk + halo (green), warm disk (red) and cool disk (cyan) clouds of the Milky Way (Savage & Sembach 1996). Filled circles represent our data points, which are best fitted by the warm halo cloud pattern.

cannot be resolved in a spectrum, regardless of resolution and S/N.

We stress that the availability of simultaneous high and low resolution spectra of a GRB afterglow is an extremely rare event. In this context, the comparison of the column densities obtained fitting the line profile of a high resolution spectrum with that estimated by the Curve of Growth analysis applied to a low resolution one could be extremely important. In fact, this can help to determine a range of column densities for which it is safe to apply the Curve of Growth analysis when high resolution data are missing. This is because high column densities can result in the saturation effect, a problem that is difficult to address using low resolution spectra only (see e.g. Penprase et al. 2010). Prochaska (2006) widely discuss the limits and perils of the COG analysis applied to low resolution data. They find that this kind of analysis tends to underestimate the column densities of the absorbing species. This is because strong transitions drive the COG fit since the relative error associated to their  $W_r$  is smaller than that for weak ones. Nevertheless, strong transitions are more affected by saturation, and in order to match their observed column densities, the COG fit is forced towards high values of the effective Doppler parameter. High resolution data often show that the main contribution to the column density of strong transitions comes from one narrow component. On the other hand, the main contribution to the  $W_r$  comes from other components which account for a small fraction of the column density. These inferred high values for the effective Doppler parameter are thus mimicking a more complex situation, with the result of underestimating the real column densities. For what concerns GRB 081008 the UVES observations show no or just mild saturation even for the strongest transitions, and the two main components give a similar contribution to the total column densities. This is the reason why there is a good agreement between COG

analysis of low resolution data and line fitting analysis of high resolution ones for this particular GRB (within  $3\sigma$  in the worst cases).

Finally, we detect two weak intervening systems in our spectra. The first one is a CIV absorber in the FORS2 spectrum at  $z = 1.78$ , and the second one is a MgII system in the UVES spectrum at  $z = 1.286$ . This last system has  $W_r(MgII\lambda 2796) = 0.3\text{\AA}$ , the detection limit being  $0.1\text{\AA}$  at the  $2\sigma$  confidence level. The redshift path analyzed for MgII is  $z = 0.18 - 0.38$  and  $z = 0.71 - 1.43$  for the UVES spectrum, and  $z = 0.36 - 1.21$  for the FORS2 one.

## ACKNOWLEDGMENTS

We thank an anonymous referee for a deep and critical reading of the paper, which strongly increased its quality. This work was partially supported by ASI (I/1/011/07/0).

## REFERENCES

- Asplund, M., Grevesse, N.; Sauval, A.J. & Scott, P. 2009, *ARA&A*, 47, 481
- Ballester, P., Modigliani, A., Boitquin, O., et al.: 2000, *ESO Messenger*, 101, 31
- Campana, S., Thöne, C.C., de Ugarte Postigo, A. et al. 2010, *MNRAS*, 402, 2429
- Cobb, B.E., 2008, *GCN Circ*, 8356
- Cucchiara, A. et al. 2008, *GCN Circ* 8346
- Cucchiara, A. et al. 2008, *GCN Circ* 8372
- Dekker, H, D’Odorico, S, Kaufer, A., Delabre, B., Kotzłowski, H. 2000, *SPIE*, 4008, 534
- D’Avanzo, P. et al. 2008, *GCN Circ*, 8350
- D’Elia, V., Fiore, F., Meurs, E.J.A. et al. 2007, *A&A* 467, 629
- D’Elia, V., Fiore, F., Perna, R. et al. 2009a, *ApJ*, 694, 332
- D’Elia, V., Fiore, F., Perna, R. et al. 2009b, *A&A* 503, 437
- D’Elia, V., Fynbo, J.P.U, Covino, S. et al. 2010, *A&A*, 523, 36
- Fynbo, J.P.U., Starling, R.L., Ledoux, C. et al. 2006, *A&A*, 451, L47
- Fynbo, J.P.U., Prochaska, J.X, Sommer-Larsen, J., Dessauges-Zavadsky, M., Moller, P. 2008, *ApJ*, 683, 321
- Fynbo, J.P.U., Jakobsonn, P., Prochaska, J.X. et al. 2009, *ApJS*, 185, 526
- Ledoux, C., Vreeswijk, P.M., Smette, A. et al. 2009, *A&A*, 506, 661
- Morton, D.C. 2003, *ApJS*, 149, 205
- Noterdaeme, P, Ledoux, C., Petitjean, P., Srianand, R. 2008, *A&A*, 481, 327
- Penprase, B.E., Prochaska, J.X., Sargent, W.L.W., Toro Martines, I., Beeler, D.J. 2010, *ApJ*, 721, 1
- Perna, R., Lazzati, D., Fiore, F. 2003, *ApJ*, 585, 775
- Prochaska, J.X. 2006, *ApJ*, 650, 272
- Prochaska, J.X., Chen, H.W., Bloom, J.S. 2006, *ApJ*, 648, 95
- Prochaska, J.X., Chen, H.W., Dessauges-Zavadsky, M., Bloom, J.S. 2007, *ApJ*, 666, 267
- Prochaska, J.X., Sheffer, Y., Perley, D.A. et al. 2009, *ApJ*, 691, 27L
- Racusin, J.L. et al. 2008, *GCN Circ*, 8344
- Savage, B.D., Sembach, 1996, *ARA&A*, 34, 279
- Savaglio, S. 2000, in *IAU Symp. 204, The Infrared Background and Its Cosmological Implications*, ed. M. Harwit & M.G. Hauser (San Francisco: ASP), 307
- Savaglio, S., Fall, S.M., Fiore, F. 2003, *ApJ*, 585, 638
- Savaglio, S., Glazebrook, K., Crampton, D. et al. 2004, *ApJ*, 602, 51

- Savaglio, S., Glazebrook, K., Le Borgne, D. et al. 2005, ApJ, 635, 260
- Savaglio, S. 2006, New J. Phys, 8, 195
- Savaglio, S., Glazebrook, K. & Le Borgne, D. 2009, ApJ, 691, 182
- Schady, P., Savaglio, S., Krühler, T., Greiner, J. Rau, A. 2011, A&A, 727, 5
- Shapley, A.E., Steidel, C.C., Pettini, M., Adelberger, K.L. 2003, ApJ, 588, 65
- Sheffer, Y., Prochaska, J.X., Draine, B.T., Perley, D.A., Bloom, J.S. 2009, ApJ, 701, L63
- Spitzer, L. 1978, Physical processes in the interstellar medium, ed. L. Spitzer
- Steidel, C.C., Adelberger, K.L., Giavalisco, M., Dickinson, M., Pettini, M. 1999, ApJ, 519, 1
- Thöne, C.C., Campana, S., Lazzati, D. et al. 2011, MNRAS, 414, 479
- Tumlinson, J., Prochaska, J.X., Chen, H.-W., Dessauges-Zavadsky, M., Bloom, J.S. 2007, ApJ, 668, 667
- Vreeswijk, P.M., Ellison, S.L., Ledoux, C. et al. 2004, A&A, 419, 927
- Vreeswijk, P.M., Ledoux, C., Smette, A. et al. 2007, A&A, 468, 83
- Vreeswijk, P.M. 2011, In “GRB as Probes: From the Progenitor’s Environment to the High Redshift Universe”, Como, 16-20 May, 2011
- Yuan, P., Schady, P., Racusin, J.L. et al. 2010, ApJ, 711, 870 (Y10)